Check for updates

Possible links with methane seepage and gas hydrate dynamics inferred from authigenic barite records in the northern south china sea

Junxi Feng[1,2,3,4], Min Luo[5], Jinqiang Liang[1,2,4], Shengxiong Yang[1,2], Hongbin Wang[6], Niu Li[7]* and Xiaoming Sun[3]*

[1]MLR Key Laboratory of Marine Mineral Resources, Guangzhou Marine Geological Survey, Guangzhou, China, [2]Southern Marine Science and Engineering Guangdong Laboratory (Guangzhou), Guangzhou, China, [3]School of Marine Sciences, Sun Yat-sen University, Guangzhou, China, [4]Natural Gas Hydrate Engineering Technology Center, China Geological Survey, Guangzhou, China, [5]Shanghai Engineering Research Center of Hadal Science and Technology, College of Marine Sciences, Shanghai Ocean University, Shangha, China, [6]Qingdao Institute of Marine Geology, China Geological Survey, Qingdao, China, [7]Key Laboratory of Ocean and Marginal Sea Geology, South China Sea Institute of Oceanology, Innovation Academy of South China Sea Ecology and Environmental Engineering, Chinese Academy of Sciences, Guangzhou, China

Numerous methane seepage events occurred in periods of low or falling sea level since 330 ka BP, which is attributed to decrease in hydrostatic pressure and subsequent gas hydrate dissociation in the northern South China Sea (SCS). The seepage intensity likely decrease due to gas hydrate stabilization once there was a relatively high-stand sea level. However, there are few geochemical records of decline in upward methane flux in the northern South China Sea. Here, combing porewater and solid-phase analyses, the geochemical cycling of barium was investigated in two piston cores from sites HD109 and HD319 within two areas with inferred gas hydrate occurrence in the Taixinan Basin of the northern SCS, in order to track the net decrease in the upward methane flux and to estimate the total duration time of these events in the studied sediments. The results indicate that there are four intervals with barium enrichments in the sediment section overlying the occurrent sulfate-methane transition zone (SMTZ) at both cores, suggesting the SMTZs have downward migrated through time. Based on the excess barium contents and the diffusive Ba^{2+} fluxes above the current SMTZ, we estimate the total time for barium accumulation at both cores is about ten thousand years. It is suggested that some methane seepage events temporarily enhance the upward flux of methane, inducing anaerobic oxidation of methane and associated SMTZ close to the sediment surface before the Holocene. After the most intensive seepage event ceased in the post-glacial period, the upward methane flux decreased and the SMTZ migrated downward gradually, preserving enrichments of diagenetic barite. Overall, these new data confirm the episodic decrease in upward methane flux recorded by authigenic barite after the last glacial maximum, which is likely related to the stabilization of underlying gas hydrate reservoir. This study may fill in the gap of the

geochemical records of the variations in methane seepage and gas hydrate system during the post-glacial period in the northern SCS.
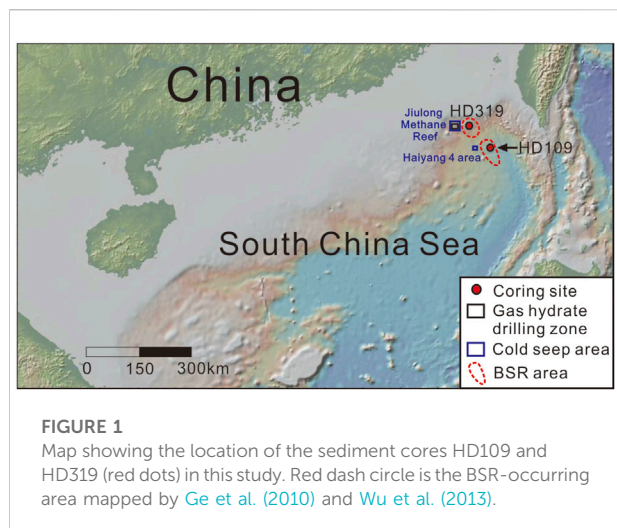
Introduction

Substantial amounts of methane existing as dissolved and free gas, as well as ice-like gas hydrates are hosted within the sediments in continental margins (Judd and Hovland, 2007). Dissolved and free gas can migrate from underlying reservoirs to the subsurface sediments through specific fluid conduits like faults and fractures (Boetius and Wenzhöfer, 2013). The majority of dissolved methane upward migrated is consumed by anaerobic oxidation of methane (AOM) mediated by a microbial consortium in the sulfate-methane transition zone (SMTZ) where both seawater sulfate and methane are consumed (AOM: $CH_4 + SO_4^{2-} \rightarrow HCO_3^- + HS^- + H_2O$) (Barnes and Goldberg, 1976; Boetius et al., 2000; Wu et al., 2022). The AOM typically induces formation of several types of authigenic minerals including carbonate (e.g., Peckmann and Thiel, 2004), pyrite (e.g., Peckmann et al., 2001) and barite (e.g., Torres et al., 1996; Torres et al., 2003; Castellini et al., 2006; Feng and Roberts, 2011).

Authigenic barite is widely used as a valuable proxy for tracing past methane fluxes in marine sediments (Dickens, 2001; Griffith and Paytan, 2012). The barium in authigenic barite is mostly derived from biogenic barite particles which form in the water column during the decomposition of organic substances and are transported to the seafloor. The sedimentary barite particles become undersaturated and decompose into barium (Ba^{2+}) and sulfate (SO_4^{2-}) ions when they are buried below the SMTZ. The released Ba^{2+} then migrates upward and enters the sulfate-bearing zone where authigenic barites form again just above the SMTZ ($Ba^{2+} + SO_4^{2-} \rightarrow BaSO_4$; Torres et al., 1996). The diagenetic barite is significantly different in the size from normal microcrystalline biogenic particles, especially in methane-rich sediments where it can grow to as large as several 10 μm (Torres et al., 1996). Sometimes at active methane seeps, massive barite deposits, e.g., chimneys, as high as 10 m in height can form on the seafloor (Greinert et al., 2002). Therefore, massive authigenic barite and barium element enrichments in sediment column can be utilized as a useful proxy to constrain the changes in the position of SMTZ and the duration time of methane release activities in the geological past (e.g., Dickens, 2001; Riedinger et al., 2006; Snyder et al., 2007a; Snyder et al., 2007b; Nöthen and Kasten, 2011; Kasten et al., 2012; Sauer et al., 2017; Schneider et al., 2018; Yao et al., 2020; Wood et al., 2021). Interestingly, significant barium enrichments occurred widespreadly at

the times of some huge paleo-climatic perturbations, including the Paleocene-Eocene thermal maximum (Dickens et al., 2003), Permian-Triassic extinction (Burger, et al., 2019), and Ediacaran Shuram excursion (Cui et al., 2021). The formation of these barium enrichments may be attributed to massive input of dissolved barium from subsurface gas hydrate reservoirs due to gas hydrate dissociation and further authigenic barite precipitation (Dickens et al., 2003; Burger, et al., 2019; Frieling et al., 2019).

There are widespread methane-rich fluid seepages on the northern continental slope of the South China Sea (SCS) as uncovered by authigenic carbonates sampled at over thirty sites (Feng et al., 2018). There are only two active seep areas–"Haima seeps" and "Site F" found in the northern SCS so far (Feng and Chen, 2015; Liang et al., 2017). The majority of the authigenic carbonates in the northern SCS precipitate either during the periods of sea-level lowstands or corresponding to the times with falling sea-level prior to the Last Glacial Maximum (LGM) (Tong et al., 2013; Han et al., 2014; Yang et al., 2018; Maoyu Wang et al., 2022). It is thus suggested that gas hydrate dissociation took place during sea-level lowstands or falling stages resulting from reduced hydrostatic pressures, which in turn led to methane seepage and formation of authigenic minerals close to the seafloor in the northern SCS (Tong et al., 2013; Han et al., 2014; Li et al., 2016; Lin et al., 2016; Xie et al., 2019). At the post-glacial age, the upward methane flux seemed to decrease significantly on a regional scale (Lin et al., 2016). However, extensive seep activities also occurred during the sea-level highstand associated with Marine Isotope Stage (MIS) 5e (133.3–112.7 ka BP) and MIS 1 (since 14 ka BP) (Feng and Chen, 2015; Liang et al., 2017; Chen et al., 2019). These seepage events derived from gas hydrate dissociation were probably attributed to a climate-driven rise in bottom water temperature (Chen et al., 2019). The mechanisms controlling seepage activity are still controversial. More geochronologic evidences, especially the records of decline in upward methane flux during the deglaciation periods, are required to better understand the driving mechanisms. To date, there are few reports on this kind of geochemical records (e.g., Luo et al., 2015; Lin et al., 2016; Hu et al., 2017), which limits our understanding of the evolution of subsurface methane release in the northern SCS.

In this study, we investigate the downcore variation in Ba content in the sediments and dissolved porewater Ba^{2+} concentrations in two piston cores HD109 and HD319 in

FIGURE 1
Map showing the location of the sediment cores HD109 and HD319 (red dots) in this study. Red dash circle is the BSR-occurring area mapped by Ge et al. (2010) and Wu et al. (2013).

the northeastern SCS, in order to trace the changes in the position of SMTZ and access the present-day and past upward methane fluxes. A numerical transport-reaction model is used to stimulate the geochemical data of pore fluids in order to estimate the present-day methane fluxes. The data of Ba content in both pore fluids and sediments are used to calculate the time required for the formation of authigenic barium enrichments at both sites.

Geological background

The northern SCS is classified as a Cenozoic passive continental margin. The study area is located on the lower slope and at the bottom of the Taixinan Basin (Figure 1) (McDonnell et al., 2000; Suess, 2005). The thickness of sediment in the Taixinan Basin can reach 10 km, where complex faults, fractures, and mud diapirs are well developed. Thus, these conditions favor methane-rich fluid seepage and gas hydrate accumulation (McDonnell et al., 2000; Suess, 2005; Wu et al., 2007). Widespread bottom simulating reflectors (BSR) representing the bottom of the gas hydrate stability zone was observed (e.g., McDonnell et al., 2000; Suess, 2005; Li et al., 2013; Li et al., 2015; Kuang et al., 2018; Bai et al., 2019). In addition, plenty of seep sites have been discovered in this region with water-depth ranging from ~200 to ~3,300 m, including the giant Jiulong Methane Reef with seep carbonates covering ~430 km², the Haiyang four area as well as the Site F with active seepage (e.g., Chen et al., 2005; Suess, 2005; Han et al., 2008; Tong et al., 2013; Xudong Wang et al., 2022). Abundant gas hydrates in shallow sediments were successfully recovered from the Jiulong Methane Reef area (Zhang et al., 2015), which validated that methane-rich fluid seepage and gas hydrates were common along the passive margin of the Taixinan Basin.

Materials and methods

Sampling and analytical methods

Two piston cores (HD109 and HD319) were retrieved from two areas with BSR occurrence in the Taixinan Basin during the cruises of the R/V "*Haiyang IV*" in 2003 and 2004, respectively. Site HD109 is located at the bottom of the Taixinan Basin, whereas site HD319 is located on the lower continental slope of this basin (Figure 1). The coordinate positions of these sites were shown in Chen et al. (2006). The lengths of the cores are 771 and 730 cm, respectively (Table 1). The sediments at these cores consist mainly of dark-green, unconsolidated clayey silt and silty clay with several quartz grains. The sand contents are 3 and 1% at the cores HD109 and HD319, respectively, which are much lower than that of the turbidite deposit at nearby site. Therefore, there are only normal deep-sea sediments at the two cores (Chen et al., 2006).

After collection, the engineers cut the cores into sections at intervals of 100 cm from top to bottom, and stored them in a cold room (4℃). The top 20 cm sediments of each sediment section were used to measure headspace gas contents onboard. Around 10 ml of sediments were put into 20-ml empty vials onboard to replace the 10-ml headspace required for the chromatograph injection. The hydrocarbon gas concentrations were measured onboard using the gas chromatograph method (Agilent 7890N). The precision for methane concentration was ±2.5%.

After retrieval of the cores HD109 and HD319, porewater samples were immediately collected from slices of the cores at intervals of 100 cm via a pumping vacuum extraction device at room temperature, then transferred to sealed plastic bottles and stored at 4 ℃ in April 2003 and May 2004, respectively. Porewater samples of the core HD109 were collected again for further study at intervals of 20 cm after the cruise in May 2003. The offshore analyses of porewater samples were performed at Nanjing University in August 2003 and September 2004, respectively. Dissolved sulfate (SO_4^{2-}) and calcium ion (Ca^{2+}) were determined by the standard methodology of ion chromatography (Metrohm 790 IC). The relative standard deviation was less than 2%. The concentrations of Ba^{2+} and I in porewater samples were analyzed by inductively coupled plasma mass spectrometry (ICP-MS, Finnigan Element II). Before measurement, samples were prepared by diluting in 2% HNO_3 (for Ba^{2+}) or aqua ammonia (for I) with rhodium (Rh) as an internal standard. The analytical precisions were calculated to be <5% for Ba and <2% for I.

The calcium (CaO), aluminium (Al_2O_3) and silicon (SiO_2) contents of the sediment samples were measured *via* PANalytical AXIOSX X-ray fluorescence spectrometry. The analytical precisions were smaller than 2%. After digesting the sediment samples via HCl, HF, and $HClO_4$ acid mixture, the total contents of Ba in sediments were measured via a PerkinElmer Optima 4300DV ICP-OES. The analytical precision was better than 2%.

TABLE 1 Location of the studied sites.

Site	Water depth (m)	Bottom water temperature	Core length (cm)
HD109	3218	~2	771
HD319	1730	~3	730

The contents of total organic carbon (TOC) were analyzed via the potassium dichromate wet oxidation method, with the relative standard deviation better than 1.5%.

Numerical modelling

A 1-D, steady-state, reaction-transport model is used to simulate the depth profiles of solid-phase particulate organic carbon (POC), headspace CH_4, dissolved SO_4^{2-}, Ca^{2+} and Ba^{2+} concentration. The model is based on the following partial differential equations for solid (Eq. 1) and dissolved (Eq. 2) species (Berner, 1980; Wallmann et al., 2006):

$$(1 - \Phi) \frac{\partial C_s}{\partial t} = - \frac{\partial ((1 - \Phi) \cdot v_s \cdot C_s)}{\partial x} + (1 - \Phi) \cdot \Sigma R \quad (1)$$

$$\Phi \frac{\partial C_d}{\partial t} = \frac{\partial \left(\Phi \cdot D_s \cdot \frac{\partial C_d}{\partial x} \right)}{\partial x} - \frac{\partial \left(\Phi \cdot v_p \cdot C_d \right)}{\partial x} + \Phi \cdot \Sigma R + \Phi$$
$$\cdot \alpha (C_0 - C_l) \quad (2)$$

where C_s and C_d (μmol cm^{-3}) is the concentration of solid and dissolved species, respectively, x (cm) is depth, t (yr) denotes time, Φ denotes porosity, D_s (cm^2 yr^{-1}) denotes the molecular diffusion coefficient corrected for tortuosity, v_p (cm yr^{-1}) denotes the burial velocity of porewater, v_s (cm yr^{-1}) denotes the burial velocity of solids, ΣR is the sum of the rates of biogeochemical reactions considered in the model, α is the mixing rate of bottom water and porewater, C_0 and C_l are the solute concentrations at the sediment-water interface (SWI) and at any depth within the mixing zone, respectively.

Porosity was assumed to decrease with depth under steady-state compaction:

$$\Phi = \Phi_f + \left(\Phi_0 - \Phi_f \right) \cdot e^{-px} \quad (3)$$

where Φ_0 and Φ_f (both dimensionless) are the porosity at SWI and below the depth of compaction, respectively. Moreover, p (cm^{-1}) is the attenuation coefficient for porosity. Since externally imposed fluid advection at the SWI is absent, the velocity of porewater and solids is directed downward under steady-state compaction relative to the SWI:

$$v_p = \frac{\Phi_f \cdot \omega}{\Phi} \quad (4)$$

$$v_s = \frac{\left(1 - \Phi_f \right) \cdot \omega}{1 - \Phi} \quad (5)$$

where ω (cmyr^{-1}) denotes the sedimentation rate.

Depth-dependent molecular diffusive coefficients of dissolved species are calculated based on the equation of Boudreau (1997):

$$D_s = \frac{D_m}{1 - ln \ (\Phi)^2} \quad (6)$$

where D_m is the molecular diffusion coefficient at the local temperature, salinity and pressure.

The irrigation rate α, is described as a non-local transport of solutes:

$$\alpha = \alpha_0 \cdot \frac{\exp \ (L_{irr} - x / \alpha_1)}{1 + \exp \ (L_{irr} - x / \alpha_1)} \quad (7)$$

where α_0 (yr^{-1}) denotes the irrigation intensity coefficient, L_{irr} (cm) is the maximum depth of irrigation, α_1 (cm) is the parameter pointing to the degree of attenuation for bubble irrigation just below the depth of L_{irr}.

The dominant biogeochemical reactions included in the model are organoclastic sulfate reduction (OSR), AOM, *in situ* methanogenesis (MG), and authigenic carbonate precipitation (CP). This model does not consider the reactions of authigenic barite precipitation and dissolution. Instead, the differences between the measured and modelled depth profiles of Ba^{2+} concentration, is used to trace the diagenetic reactions of barite at times of sampling (cf. Vanneste et al., 2013). Additionally, other reactions, including aerobic respiration, denitrification, iron reduction, and manganese reduction via organic matter remineralization are not considered in the model as these processes only occur within the top of sediment (~10–20 cm below the SWI). The reaction rate expressions are shown in Table 2, and the net reaction terms of one solid (POC) and three dissolved species (SO_4^{2-}, Ca^{2+} and CH_4) are given in Table 3. All the parameters in the model are shown in Table 4.

The simulating length of the cores are 1,000 cm for HD109 and 1,500 cm for HD319, respectively. Measured values at the top of sediment are used as upper boundary conditions for all species (Dirichlet boundary). A zero concentration gradient (Neumann-type boundary) was set at the lower boundary for all the species except for Ba^{2+}. The lower boundary condition for Ba^{2+} is imposed as a fixed value. The model was calculated by the NDSolve object of

TABLE 2 Kinetic reaction rate laws in the model.

Rate	Kinetrc rale law[a]
Total POC degradation (wt% C yr^{-1})	$R_{POC} = (0.16 \cdot (a_0 + \frac{x}{v_s})^{-0.95} \cdot POC$
Organic matter degradation by sulfate reduction (mmol cm^{-3} yr^{-1} of SO$_4^{2-}$)	$R_{OSR} = 0.5 \cdot R_{POC} \cdot \frac{[SO_4^{2-}]}{[SO_4^{2-}]+K_{SO_4^{2-}}}/f_{POC}$
Methanogenesis (mmol cm^{-3} yr^{-1} of CH$_4$)	$R_{MG} = 0.5 \cdot R_{POC} \cdot \frac{K_{SO_4^{2-}}}{[SO_4^{2-}]+K_{SO_4^{2-}}}/f_{POC}$
Anaerobic oxidation of methane (mmol cm^{-3} yr^{-1} of CH$_4$)	$R_{AOM} = k_{AOM} \cdot [SO_4^{2-}][CH_4]$
Authigenic carbonate precipitation (mmol cm^{-3} yr^{-1} of Ca^{2+})	$R_{CP} = k_{Ca} \cdot (\frac{[Ca^{2+}]\cdot[CO_3^{2-}]}{K_{SP}} - 1)$

[a]Notation: R_{POC} (wt% C yr^{-1}): POC degradation rate, a_0 (yr): initial age of organic matter in uppermost sediment, v_s (cm yr^{-1}): burial velocity of solids, x (cm): depth in the sediment, Kc: inhibition constant for POC degradation, POC (wt%): POC content in sediment. R_{OSR} (mmol cm^{-3} yr^{-1} of SO$_4^{2-}$): OSR rate, [SO$_4^{2-}$]: SO$_4^{2-}$ concentration, $K_{SO_4^{2-}}$: Michaelis–Menten constant for the inhibition of sulfate reduction at low sulfate concentrations, f_{POC}: convert between POC (wt%) and DIC (mmol cm^{-3} of pore fluid). f_{POC}= MW$_C$/10Φ/(1−Φ)/ρ_S, where MW$_C$ is the molecular weight of carbon (12 g mol^{-1}), ρ_S is the density of dry sediments, and Φ is the porosity. R_{MG} (mmol cm^{-3} yr^{-1} of CH$_4$): methanogenesis rate. R_{AOM} (mmol cm^{-3} yr^{-1} of CH$_4$): AOM rate, k_{AOM}: rate constant of AOM, [CH$_4$]: dissolved CH$_4$ concentration. R_{CP} (mmol cm^{-3} yr^{-1} of Ca^{2+}): authigenic carbonate precipitation rate, k_{Ca} (molcm^{-3} yr^{-1}): rate constant of CP, K_{SP} (mol^2·l^2): thermodynamic equilibrium constant at the seafloor condition, [Ca^{2+}] and [CO$_3^{2-}$]: Ca^{2+} and CO$_3^{2-}$ concentrations, respectively.

TABLE 3 Reaction terms of species considered in the model.

Species	Rate
Particulate organic carbon (POC)	$- R_{POC}$
Sulfate (SO$_4^{2-}$)	$- R_{OSR} - R_{AOM}$
Calcium (Ca^{2+})	$- R_{CP}$
Methane (CH$_4$)	$R_{MG} - R_{AOM}$

MATHEMATICA V. 12.0. All simulations were run for 10^6 years to reach steady state with a mass conservation of >99 %.

Estimating the time for authigenic barite accumulation

The background Ba content (C_0) is about 440 ± 10 mg kg^{-1} and 500 ± 10 mg kg^{-1} at the cores HD109 and HD319, respectively (Figure 3). Using this content as the lower limit, the depth-integrated total amount of excess Ba in the barium enrichment layer was obtained by the expression below:

$$S_{Ba} = \int_u^v (C_x - C_0) \cdot \rho \cdot (1 - \Phi)dx \qquad (8)$$

where C_x is the barium content within the peaks from a depth interval from u to v, ρ and Φ are the average grain density and porosity of the sediments.

To calculate the diffusive Ba^{2+} fluxes throughout the SMTZ, Eqs. (9) was used assuming a steady state condition (Schulz, 2006):

$$J_{Ba} = -\Phi D_s \frac{dC_{Ba}}{dx} \qquad (9)$$

where J_{Ba}: Ba^{2+}diffusive flux (μmol m^{-2} yr^{-1}), Φ: porosity of sediment, D_S: diffusion coefficient of sediment (m^2 s^{-1}), C_{Ba}: Ba^{2+} concentration (μmol L^{-1}), and x: sediment depth (m). Averages of sediment porosity from 0.65 to 0.75 is applied (Suess, 2005; Huang et al., 2008). The diffusion coefficient D_s is calculated from the diffusion coefficient in free solution (D_0) of 4.41×10^{-6} cm^2 s^{-1} (2 °C) for HD109 and 4.59×10^{-6} cm^2 s^{-1} (3 °C) for HD319, according to Schulz (2006).

Under the assumption of a constant upward Ba^{2+} flux into the sulfate reduction zone, the time (t) required to precipitate the barium pool was calculated as below:

$$t = S_{Ba}/J_{Ba} \qquad (10)$$

Results

Geochemical trend of pore fluids

Depth profiles of headspace CH$_4$, porewater SO$_4^{2-}$, Ca^{2+}, Ba^{2+}, I concentrations and $\delta^{13}C_{CH4}$ or $\delta^{13}C_{DIC}$ at cores HD109 and HD319 are presented in Figure 2, and the specific data are provided in Table 5. At core HD109, the SO$_4^{2-}$ concentrations keep almost constant as about 28 mM except four abnormal values above 350 cmbsf. Below this depth, it gradually declines to 1.9 mM at the depth of 680 cmbsf and remains at this low level till the base of the cor (Figure 2A). The CH$_4$ concentrations remain at low levels (0.4–2.1 μM) above 520 cmbsf, followed by a rapid increase to 239.4 μM at 771 cmbs (Figure 2A). The Ca^{2+} concentrations keep relatively constant at the seawater value (~10 mM) with some degree of variations above 300 cmbsf and then decrease to 2.2 mM at 750 cmbsf with some abnormal peaks below 600 cmbs (Figure 2B). The dissolved

TABLE 4 The dataset of specific parameters and boundary conditions used in the model.

Parameter	HD109	HD319	Unit
Temperature (T)[a]	2	3	°C
Salinity (S)	35	35	PSU
Pressure (P)	32.7	17.6	MPa
Density of dry solids (ρ_s)	2.6	2.6	g cm^{-3}
Density of porewater (ρ_{pw})	1.033	1.033	g cm^{-3}
Sedimentation rate (ω)[b]	0.01	0.01	cm yr^{-1}
Porosity at sediment-water interface (Φ_0)[c]	0.7	0.7	
Porosity in compacted sediments (Φ_f) [c]	0.7	0.7	
Depth attenuation coefficient for porosity (p)	0	0	cm^{-1}
Initial age of POC (a_0)[d]	50	50	Kyr
Michaelis–Menten constant for POC degradation ($K_{SO_4^{2-}}$)[e]	1×10^{-4}	1×10^{-4}	mM
Rate constant for AOM (k_{AOM})[d]	30	30	cm^3 yr^{-1} mmol^{-1}
Depth of gas bubble irrigation (L_{irr})	280	200	Cm
Irrigation coefficient at the surface (α_0)	0.1	0.1	yr^{-1}
Attenuation coefficient for decrease in bubble irrigation (α_1)[e]	5	5	Cm
Rate constant for carbonate precip./dissol. (k_{Ca})	1.3×10^{-6}	3×10^{-7}	mmol cm^{-3} yr^{-1}
Upper boundary condition for SO$_4^{2-}$	29	26	mM
Upper boundary condition for Ca^{2+}	10.3	10.3	mM
Upper boundary condition for Ba^{2+}	1.5	1.9	μM
Lower boundary condition for SO$_4^{2-}$	$\partial C/\partial x = 0$	$\partial C/\partial x = 0$	-
Lower boundary condition for Ca^{2+}	$\partial C/\partial x = 0$	$\partial C/\partial x = 0$	-
Lower boundary condition for Ba^{2+}	25	25	μM

[a]alculated using an empirical formula.
[b]Chen et al. (2006).
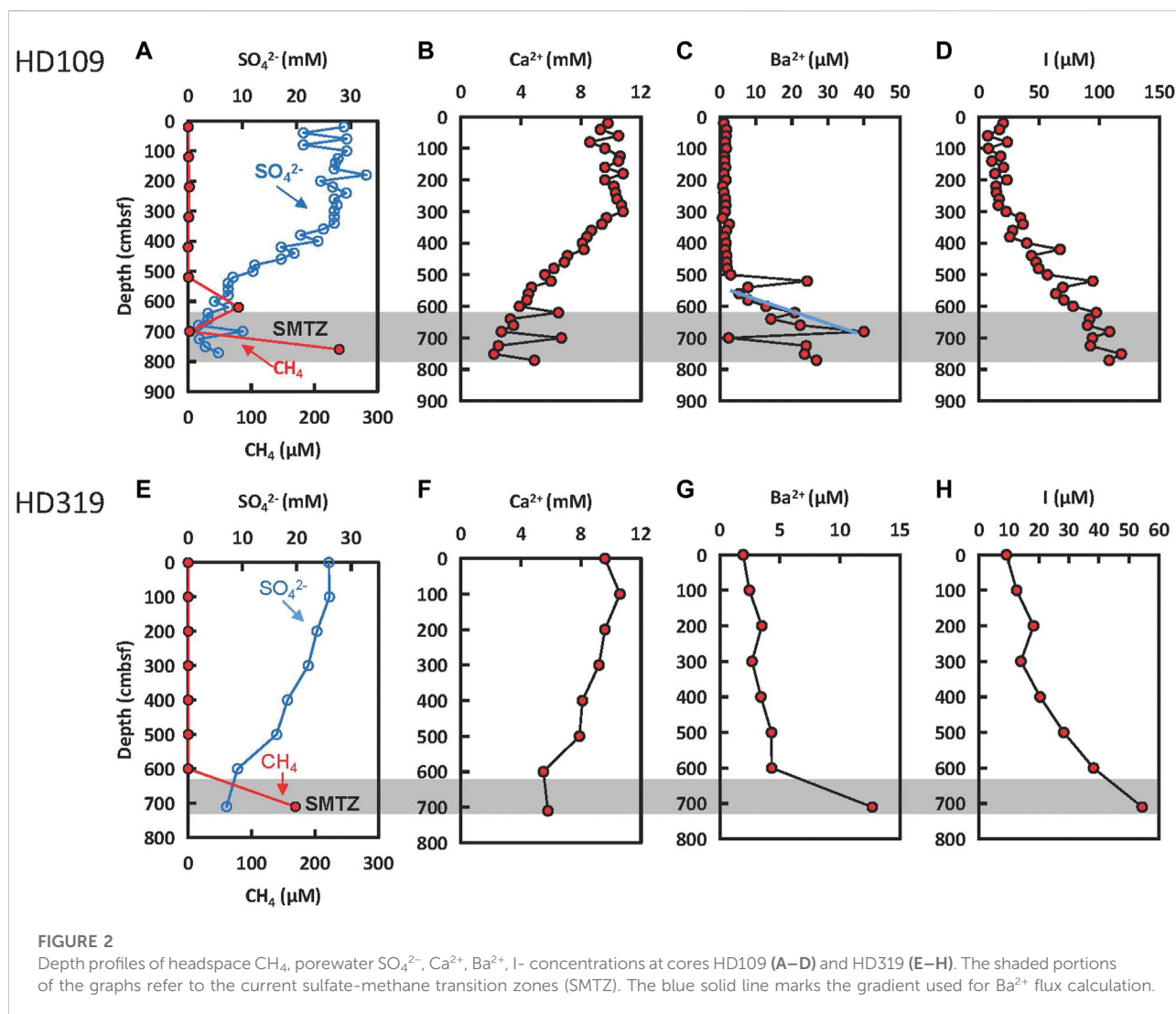[c]Wang et al. (2000).
[d]Wallmann et al. (2006).
[e]Chuang et al. (2013).

Ba^{2+} concentrations remain low (<2 μM) in the uppermost 500 cm. Below this depth, Ba^{2+} concentrations increase to highest value (40 μM) in ~680 cmbsf with some fluctuation (Figure 2C). The I concentrations are also relatively constant at a low level (~16 μM) above 300 cmbsf and increase to 108 μM at the bottom of the core with some fluctuation (Figure 2D).

Similar to core HD109, the SO$_4^{2-}$ and Ca^{2+} concentrations vary little in the upper 100 cmbsf. Below this depth, they gradually decline to 7.1 and 5.8 mM at the bottom of core HD319, respectively (Figures 2F,G). The CH$_4$ concentrations vary little from 0.2 to 0.4 μM above 600 cmbsf, followed by a sharp increase to 169.3 μM at the bottom of the corFigure 2F 2f). The dissolved Ba^{2+} concentrations remain low values in the upper 600 cmbsf and rise to the highest value (12.7 μM) at 710 cmbs Figure 2H. The dissolved I concentrations increase slightly above 300 cmbsf and then increase sharply to 54.4 μM at the bottom of the core Figure 2I.

Geochemical trend of sediments

Depth profiles of Ba content, Ba/Al ratios, CaO, Al$_2$O$_3$, SiO$_2$ and TOC contents in the sediments of cores HD109 and HD319 are presented in Figure 3, and the raw data are shown in Table 6. Total Ba contents range from 420 to 758 mg kg^{-1} at core HD109 and from 448 to 1,147 mg kg^{-1} at core HD319. The total solid-phase Ba content below 560 cmbsf of core HD109 and throughout core HD319 remains almost constant, fluctuating at 440 ± 10 mg kg^{-1} and 500 ± 10 mg kg^{-1}, and is thus assumed as the 'background' values of solid-phase Ba conten Figure 3A. Above 560 cmbsf of core HD109, the Ba contents are higher and at least four layers of Ba enrichments are recognized. The Ba contents were normalized to Al for purpose of deducting lithologic changes. The depth intervals of Ba enrichments are ca. 40–160 cmbsf, 200–240 cmbsf, 240–300 cmbsf and 320–560 mbsf, respectively. The maximum Ba concentrations in these layers are 698, 758, 596 and 595 mg kg^{-1}, respectively. Similar to core HD109, there are also four layers with Ba enrichment at the core HD319 (Figure 3F). The depth

FIGURE 2
Depth profiles of headspace CH₄, porewater SO₄²⁻, Ca²⁺, Ba²⁺, I- concentrations at cores HD109 **(A−D)** and HD319 **(E−H)**. The shaded portions of the graphs refer to the current sulfate-methane transition zones (SMTZ). The blue solid line marks the gradient used for Ba²⁺ flux calculation.

intervals of Ba enrichments are ca. 280–320 cmbsf, 400–420 cmbsf, 580–600 cmbsf and 620–660 mbsf, respectively. The maximums of Ba concentration within these zones are 1,147, 729, 905 and 944 mg kg⁻¹, respectively.

The major element contents at the core HD109 are 1.5–5.7% for CaO, 14.3–17.4% for Al_2O_3, and 54.9–61.8% for SiO_2, respectively Figures 3B–D. The contents of CaO, Al_2O_3 and SiO_2 at the core HD319 are 2.7%–8.4%, 14.3%–18.3% and 51.0–58.1%, respectively Figures 3G–I. The TOC contents range from 0.7 to 1.5% at core HD109 and from 0.6 to 1.1% at core HD319, respectively Figures 3E,J.
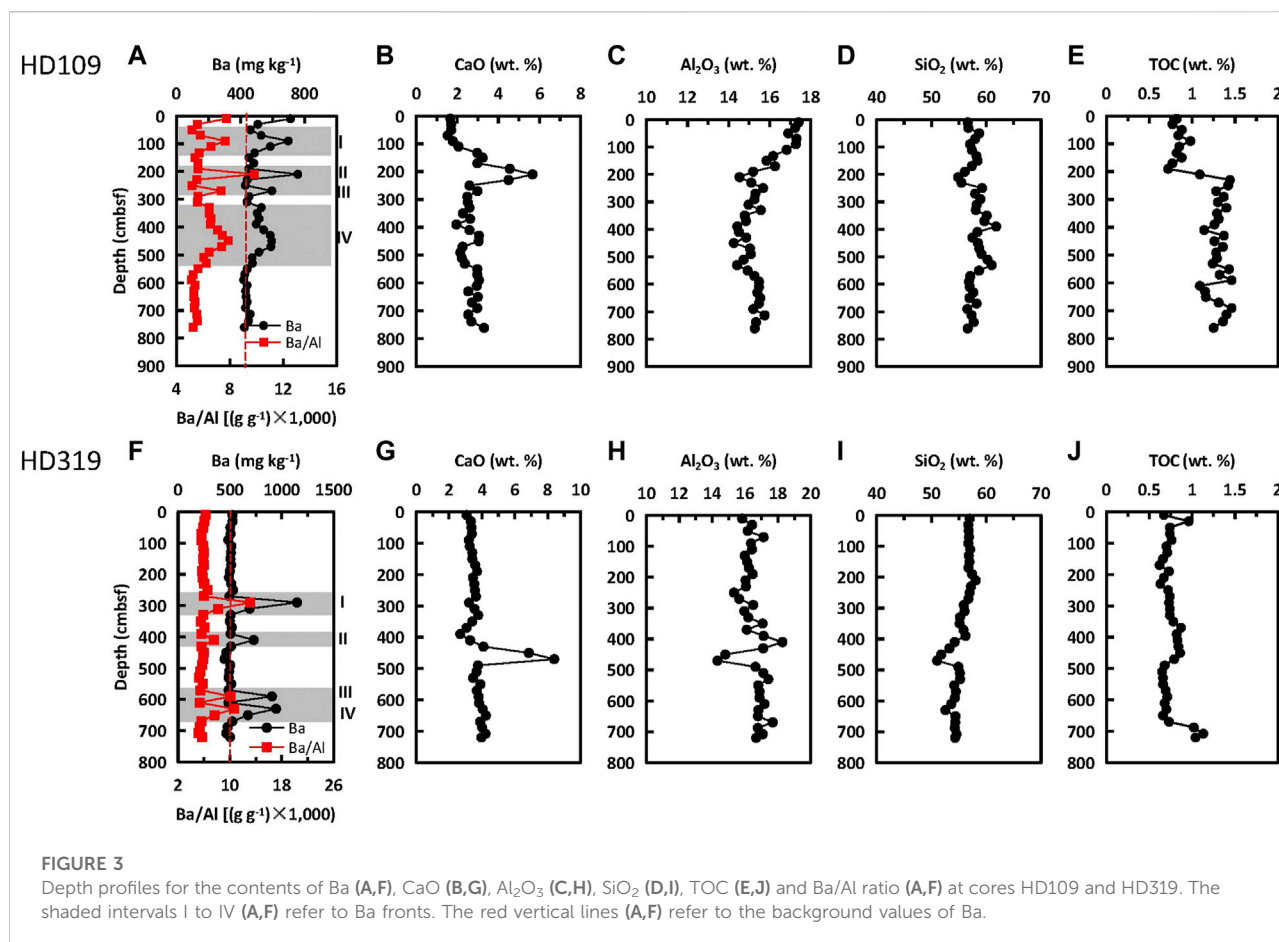
Modelling results

The modelled profiles and turnovers are exhibited in Figure 4 and Table 7, respectively. The steady-state

stimulation results matched the downcore trend of POC, SO_4^{2-}, and Ca^{2+} concentrations at the cores HD109 and HD319 with prominent differences between modelled and measured concentrations of CH_4 owing to rapid degassing at the time of sampling (Figure 4). The OSR rates were 19.4 and 21.5 mmol m⁻² yr⁻¹ for cores HD109 and HD319, respectively. In comparison, the AOM is the main pathway of sulfate reduction, which rates were 172.2 and 45.3 mmol m⁻² yr⁻¹ for the two cores, respectively. Authigenic carbonate precipitation was induced by the OSR and AOM reactions, which rates were 31.8 and 7.3 mmol m⁻² yr⁻¹ for the two cores (Table 7). Additionally, the modelled Ba^{2+} concentrations are higher than the measured Ba^{2+} values above the SMTZ at both cores, suggesting that dissolved Ba^{2+} had been taken up into the solid phase when pore fluid samples were collected. In contrast, porewater Ba^{2+} concentrations excess the modelling Ba^{2+} values at depth interval of 600–770 cmbsf of the core

TABLE 5 Headspace CH_4, porewater SO_4^{2-}, Ca^{2+}, Ba^{2+}, I^- concentrations of cores HD109 and HD319.

Core ID	Depth (cmbsf)	SO_4^{2-} (mM)	Ca^{2+} (mM)	Ba^{2+} (µM)	I (µM)	CH_4 (µM)
HD109[a]	20	28.8	9.8	1.1	20.2	0.4
	40	21.3	9.3	1.9	17.1	
	60	29.3	10.5	1.8	7.4	
	80	21.3	8.6	1.5	23.6	
	100	29.3	9.6	1.8	7.9	
	125	27.7	10.6	1.3	18	0.8
	140	27.2	10.5	1.4	10.8	
	160	27	9.6	1.6	20.4	
	180	32.9	10.8	1.2	13.3	
	200	24.5	9.6	1.7	23.3	
	220	26.7	10.2	0.8	14.2	2.1
	240	29.2	10.3	1.1	14.6	
	260	27	10.4	1.6	16.7	
	280	27.5	10.7	1.6	16.2	
	300	27	10.8	1.5	22.6	
	320	27	9.7	0.7	34.6	1.1
	340	27	9.4	2.6	36.6	
	360	25	8.7	1.8	28	
	380	20.8	8.4	1.3	25.7	
	400	24	8.1	1.7	39.7	
	420	17.2	8.2	1.5	67.4	0.2
	440	19.6	7.1	1.9	43.7	
	460	17.2	6.9	1.9	47.5	
	480	12.3	6.2	2.1	49.6	
	500	12	5.6	3.0	56.9	
	520	8.3	6	24.2	94.5	0.8
	540	7.4	4.7	7.8	69.6	
	560	7.4	4.5	5.4	63.8	
	580	7.4	4.4	7.8	70.5	
	600	4.9	3.9	12.8	78.2	
	620	7.4	6.5	20.8	97.4	80.0
	640	3.7	3.3	14.2	91.8	
	660	3.7	3.5	22.3	90.1	
	680	1.9	2.7	40.0	108.4	
	700	10.1	6.7	2.4	94.2	2.4
	725	2.1	2.5	24.0	92.5	
	751	3.2	2.2	23.5	118.1	
	771	5.6	4.9	26.8	108	239.4
HD319	0	25.9	9.6	1.9	9.2	0.2
	100	26	10.6	2.5	12.6	0.3
	200	23.7	9.6	3.5	18.2	0.4
	300	22.1	9.2	2.7	14	0.4
	400	18.3	8.1	3.4	20.4	0.4
	500	16.3	7.9	4.3	28.3	0.3
	600	9.1	5.5	4.3	38.2	0.3
	710	7.1	5.8	12.7	54.4	169.3

[a]The data of pore water SO_4^{2-} and headspace CH_4 concentrations are cited from Lin et al. (2017).

FIGURE 3
Depth profiles for the contents of Ba **(A,F)**, CaO **(B,G)**, Al$_2$O$_3$ **(C,H)**, SiO$_2$ **(D,I)**, TOC **(E,J)** and Ba/Al ratio **(A,F)** at cores HD109 and HD319. The shaded intervals I to IV **(A,F)** refer to Ba fronts. The red vertical lines **(A,F)** refer to the background values of Ba.

HD109, suggesting that Ba^{2+} had been released from the sedimentary barite to the pore fluids (c.f. Vanneste et al., 2013).

Timing of authigenic barite front accumulation

Given a fixed upward Ba^{2+} diffusive flux into the sulfate reduction zone, the accumulation time for the measured barium peaks at cores HD109 and HD319 can be estimated. Considering that porosity data are not available but are important for flux calculation, we referred to the measured porosity data in the nearby Haiyang four area (Suess, 2005; Huang et al., 2008) and applied a porosity of 65, 70, and 75% to show how sensitive the results are to the variations in porosity. The variation of the time for Ba enrichment due to different porosities is presented in Table 8. The calculation results suggest that four Ba fronts from the top to the current SMTZ at core HD109 have persisted for 2.5–4.8 ka, 1.4–2.8 ka, 0.8–1.6 ka and 4.7–9.0 ka. In addition, the duration times for the four Ba fronts from the top to

bottom at core HD319 are 3.7–7.1 ka, 1.0–1.9 ka, 1.9–3.7 ka and 3.2–6.1 ka. The calculation results underline that the barite fronts at both cores have been accumulating since the last ten thousand years, with four major peaks accumulation for several thousand years. If we take non-steady-state conditions into consideration, which include the burial input of Ba as well as the output of Ba from the front through burial, the accumulation time could be underestimated (Snyder et al., 2007b). Nevertheless, these conditions can be neglected in this study, due to the relatively short durations for each seepage events and the rather low sedimentation rates in the study area (Chen et al., 2006).

Discussion

Origin of barium fronts

Increase in solid-phase Ba contents in sediments may depend on a variety of factors. For instance, elevated Ba content might be due to high contents of aluminosilicate minerals where barium is

TABLE 6 Contents of TOC, CaO, SiO$_2$, Al$_2$O$_3$ and Ba in the sediments and Ba^{2+} concentration in pore fluids of core HD109 and HD319.

Core ID	Depth	Ba	CaO	Al$_2$O$_3$	SiO$_2$	TOC
	(cmbsf)	(mg kg^{-1})	(%)	(%)	(%)	(%)
HD109	10	712	0.8	17.4	56.6	0.82
	30	508	1.1	17.2	56.7	0.77
	50	462	0.5	16.9	58.7	0.88
	70	529	1.0	17.3	58.0	0.84
	90	698	1.1	17.3	57.0	0.98
	115	586	1.8	16.8	57.3	0.85
	130	488	2.7	16.2	58.2	0.82
	150	453	3.4	15.8	58.4	0.88
	170	483	3.9	16.3	57.3	0.77
	190	452	5.9	15.2	56.1	0.72
	210	758	7.2	14.5	54.9	1.09
	230	442	6.1	15.1	55.5	1.44
	250	430	2.7	15.7	59.2	1.42
	270	596	1.9	15.3	58.0	1.28
	290	453	1.3	15.3	58.9	1.37
	310	440	1.9	15.0	58.3	1.30
	330	530	1.8	15.6	58.1	1.40
	350	505	1.7	14.8	60.1	1.29
	370	516	1.8	14.8	59.7	1.31
	390	498	1.5	14.4	61.8	1.26
	410	544	3.6	14.5	58.4	1.14
	430	586	3.6	14.9	57.5	1.37
	450	595	3.9	14.3	58.5	1.26
	470	590	3.6	15.0	58.7	1.36
	490	515	2.5	15.1	59.1	1.28
	510	473	3.1	14.7	60.2	1.29
	530	474	2.8	14.4	61.0	1.24
	550	442	5.5	14.9	58.7	1.43
	570	426	4.9	15.3	57.1	1.32
	590	420	4.8	15.5	56.8	1.46
	610	441	4.8	15.5	57.0	1.09
	630	432	4.3	15.4	57.6	1.15
	650	435	4.8	15.5	56.9	1.16
	670	441	3.9	15.5	58.2	1.31
	690	431	4.5	15.2	56.6	1.46
	715	460	4.1	15.8	57.3	1.40
	741	450	4.3	15.3	57.7	1.36
	761	424	5.0	15.3	56.6	1.25
HD319	10	524	3.1	15.8	57.0	0.67
	30	525	3.3	16.4	56.7	0.96
	50	503	3.4	16.2	56.8	0.74
	70	507	3.4	17.1	56.8	0.74
	90	483	3.2	16.4	56.7	0.76
	110	514	3.3	16.4	57.1	0.70
	130	509	3.4	16.0	56.8	0.71
	150	504	3.4	16.1	56.9	0.66

TABLE 6 (*Continued*) Contents of TOC, CaO, SiO$_2$, Al$_2$O$_3$ and Ba in the sediments and Ba^{2+} concentration in pore fluids of core HD109 and HD319.

Core ID	Depth	Ba	CaO	Al$_2$O$_3$	SiO$_2$	TOC
	(cmbsf)	(mg kg^{-1})	(%)	(%)	(%)	(%)
	170	511	3.6	16.2	56.8	0.62
	190	499	3.7	16.5	57.4	0.73
	210	491	3.5	16.0	58.1	0.67
	230	512	3.5	16.1	57.2	0.63
	250	530	3.6	15.3	57.0	0.72
	270	495	3.6	15.6	56.7	0.74
	290	1147	3.2	16.5	55.9	0.73
	310	690	3.6	16.0	56.0	0.74
	330	507	3.8	16.2	55.2	0.74
	350	498	3.4	17.1	55.2	0.78
	370	518	3.1	16.1	55.8	0.87
	390	506	2.7	17.1	56.2	0.82
	410	729	3.3	18.3	54.2	0.83
	430	510	4.1	17.1	53.3	0.84
	450	465	6.9	14.8	51.8	0.86
	470	448	8.4	14.3	51.0	0.79
	490	503	3.8	16.6	54.9	0.68
	510	492	3.7	17.1	55.2	0.65
	530	487	3.5	17.4	55.2	0.66
	550	513	3.9	16.8	54.1	0.66
	570	486	3.7	16.9	54.4	0.69
	590	905	3.8	16.9	54.3	0.71
	610	486	3.8	17.2	53.6	0.68
	630	944	4.1	16.8	52.5	0.70
	650	674	4.2	16.8	54.4	0.66
	670	523	3.9	17.7	54.3	0.73
	688	478	4.0	16.8	54.3	1.02
	708	465	4.2	17.1	54.5	1.13
	720	501	4.0	16.7	54.3	1.04

hosted in crystal lattices. It is shown that Ba contents in detrital aluminosilicates can reach up to 1,000 mg kg^{-1} (Dymond et al., 1992). The sediments of cores HD109 and HD319 are consisted of four primary components: clay, quartz, feldspar and biogenic calcium carbonate (Chen et al., 2006). Significant variations in the distribution of these components would thus lead to marked changes in Si, Al and Ca contents in the sediments. Nevertheless, the contents of these elements do not vary considerably throughout the Ba fronts at the two cores except for the Ba fronts II at core HD109. There is a pronounced Ca peak across the Ba front (Figure 3). The Si, Al and Ca contents at core HD109 indicate normal hemipelagic background deposition and is inferred to be controlled by the glacial-interglacial cycles. An increase in the Ca contents was caused by an increase in the
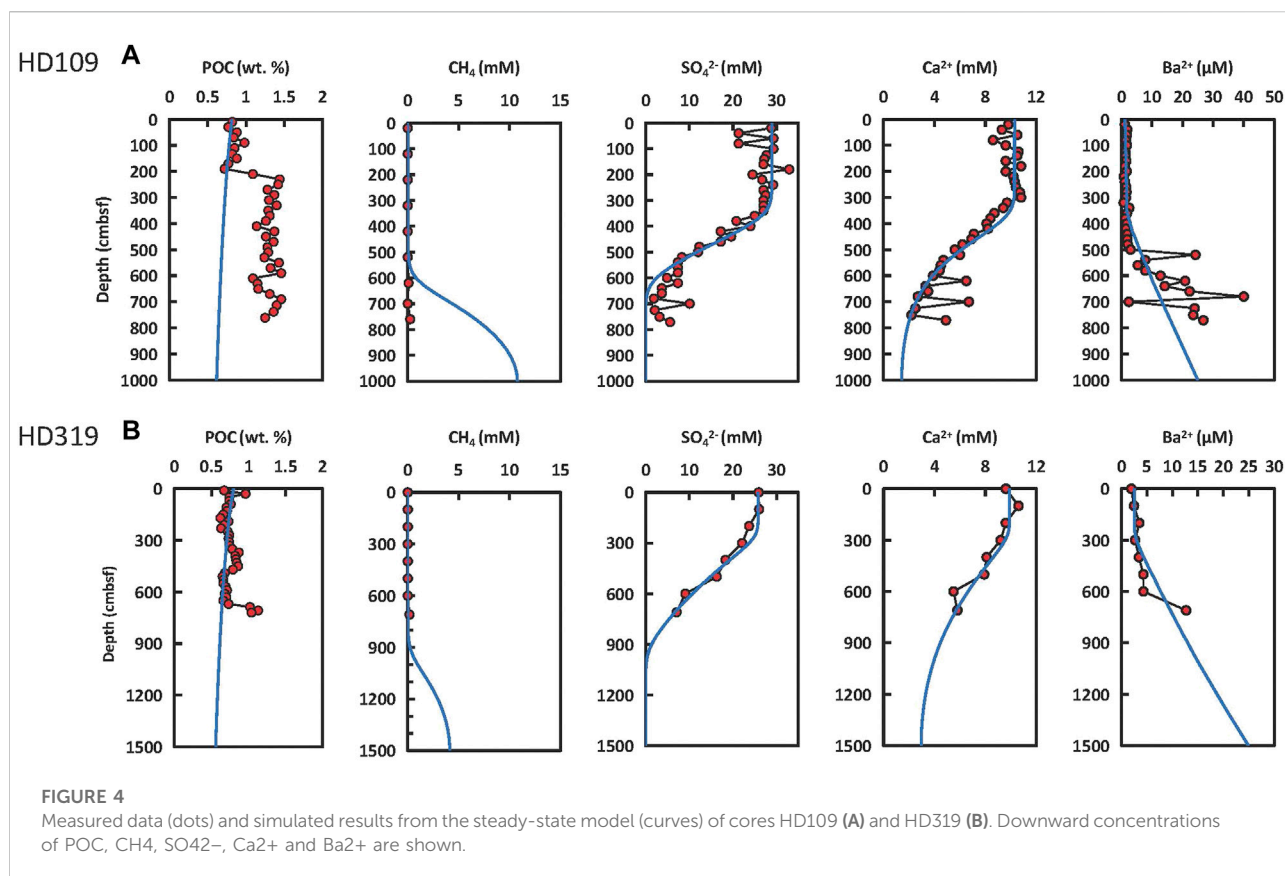
FIGURE 4
Measured data (dots) and simulated results from the steady-state model (curves) of cores HD109 **(A)** and HD319 **(B)**. Downward concentrations of POC, CH4, SO42−, Ca2+ and Ba2+ are shown.

TABLE 7 Depth-integrated turnover rates according to the steady-state modelling.

Turnover	HD109	HD319	Unit
F_{POC}: total POC mineralization	24.1	26.1	mmol m^{-2} yr^{-1} of C
F_{OSR}: sulfate reduction via POC degradation	19.4	21.5	mmol m^{-2} yr^{-1} of SO$_4^{2-}$
F_{ME}: methane formation via POC degradation	4.6	4.6	mmol m^{-2} yr^{-1} of CH$_4$
F_{GS}: methane gas dissolution	188.1	45.5	mmol m^{-2} yr^{-1} of CH$_4$
F_{AOM}: anaerobic oxidation of methane	172.2	45.3	mmol m^{-2} yr^{-1} of CH$_4$
F_{CP}: authigenic CaCO$_3$ precipitation	31.8	7.3	mmol m^{-2} yr^{-1} of C
Sulfate consumed by AOM	89.9	67.8	%
Percentage of CH$_4$ consumed by AOM	89.4	90.4	%
Percentage of CH$_4$ flux from depth	97.6	90.8	%

relative abundance of foraminifera during the transition from Pleistocene to Holocene (Chen et al., 2006). Furthermore, variations in Ba/Al ratios with depth at the two cores are virtually identical to those of solid-phase Ba contents (Figure 3), with the co-occurrence of obvious peaks of Ba content and Ba/Al ratio. The similar variation trend of the two proxies indicates that the formation of Ba fronts was not associated with variations in primary composition of sediment. In summary, the Ba contents and Ba/Al ratios for normalization

are both considerably higher than the background values at the cores HD109 and HD319 (Figure 3A,F), which implies that the Ba fronts are derived from mineral authigenesis rather than of detrital origin. Collectively, it is suggested that the Ba front is attributed to the occurrence of barite but not a Ba-rich carbonate phase (Figure 3).

The Ba of the authigenic barite is usually regarded as deriving from biogenic barite which becomes dissolved in sulfate-free pore fluids (Torres et al., 1996; McManus et al., 1998). Decaying

TABLE 8 Calculation of accumulation time of Ba fronts at cores HD109 and HD319.

Core ID	Layer	Porosity (%)	D_0 of Ba ($\times 10^{-6}$ cm^2 s^{-1})	Ba gradient[a] (mol cm^{-4})	Ba flux (mol cm^{-2} a^{-1})	Size of Ba front (g cm^{-2})	Accumulation time (ka)
HD109	I	65	4.41	3.01E−10	1.46E−08	9.73E−03	4.8
	II					5.55E−03	2.8
	III					3.19E−03	1.6
	IV					1.80E−02	9.0
							Total: 18.2
	I	70	4.41	3.01E−10	1.71E−08	8.34E−03	3.6
	II					4.76E−03	2.0
	III					2.73E−03	1.2
	IV					1.54E−02	6.6
							Total: 13.3
	I	75	4.41	3.01E−10	1.99E−08	6.95E−03	2.5
	II					3.97E−03	1.4
	III					2.28E−03	0.8
	IV					1.28E−02	4.7
							Total: 9.5
HD319	I	65	4.59	3.01E−10	1.52E−08	1.48E−02	7.1
	II					3.91E−03	1.9
	III					7.64E−03	3.7
	IV					1.28E−02	6.1
							Total: 18.8
	I	70	4.59	3.01E−10	1.78E−08	1.27E−02	5.2
	II					3.35E−03	1.4
	III					6.55E−03	2.7
	IV					1.10E−02	4.5
							Total: 13.8
	I	75	4.59	3.01E−10	2.07E−08	1.06E−02	3.7
	II					2.80E−03	1.0
	III					5.46E−03	1.9
	IV					9.17E−03	3.2
							Total: 9.8

[a]Assumed to be constant over time. Grain density: 2.6 g cm^{-3}.

biological debris induces the formation of biogenic barite particles in the water column, which then is buried in the sediments (Dymond et al., 1992; Paytan et al., 1993; Gingele and Dahmke, 1994). Hence, the fluxes of biogenic barite burial in the sediments depend on the regional productivity in the water column, and generally higher barite fluxes on the continental margins (Von Breymann et al., 1992). Correspondingly, there are elevated Ba^{2+} concentrations in the pore fluids in continental margin sediments. To date, the concentrations of porewater Ba^{2+} at the typical seep sites, such as Monterey Bay, Peru Margin, San Clemente Fault, and Carlos Ribeiro mud volcano, are considered to mainly originate from the dissolution of biogenic barite and range from 8 to 146 μM (Torres et al., 1996; Torres et al., 2002; Naehr et al., 2000; Vanneste et al., 2013). In addition, the Ba contents in the Ba fronts at the mud volcanos in the Gulf of

Mexico are as high as 14,600–23,000 mg kg^{-1}, corresponding to the very high Ba^{2+} concentration in the pore water at these sites (up to 1.2 mM) (Castellini et al., 2006). The excess Ba was released from the dissolution of detrital K-feldspar in sandstone layers (Castellini et al., 2006). In this study, the porewater barium concentrations measured at the cores HD109 and HD319 (up to ~40 μM) are within the range of biogenic barite provenance, suggesting that the dissolved barium at these cores is mainly derived from biogenic barite.

Present-day methane and barium cycle

The sulfate depletion in porewater and the elevated methane concentration at the lower section of the cores HD109 and

HD319 indicate the occurrence of sulfate reduction-driven AOM in the shallow sediments of both sites (Figure 2). There is a relatively broad zone (~600–700 cmbsf) of methane and sulfate co-existence at the core HD109. It is suggested that methane tailing in the sulfate zone may result from incomplete AOM, which may be caused by the dynamic processes of reactive intermediates related to AOM (Dale et al., 2008; Holmkvist et al., 2011).

The porewater profiles of the two cores show a kink-type feature, similar to those observed at other sites in the northern SCS (Yang et al., 2010; Chuang et al., 2013; Feng et al., 2019; Feng et al., 2020; Hu et al., 2019). As the concentrations of the primary dissolved species in porewaters above the kink are close to bottom seawater values, the plausible mechanism for the occurrence of kink-type profiles is probably attributed to seawater intrusion due to hydrological and physical processes (Hensen et al., 2003; Hong et al., 2017). By using a reaction-transport model, the dissolved methane fluxes toward the SMTZ are calculated to be 188.1 mmol m^{-2} yr^{-1} for HD109 and 45.5 mmol m^{-2} yr^{-1} for HD319, respectively (Table 7). According to the modelling results, ~90 and 68% of dissolved sulfate are consumed by AOM at cores HD109 and HD319, respectively. Moreover, the simulation results show that the depth-intergrated AOM rates at both cores are about 10–37 times of the in situ methanogenesis rates (Table 7). Hence, the relative contribution ratios of external methane source to the total methane budget are 98 and 91% at cores HD109 and HD319, respectively, indicating that the major part of methane was derived from one or more subsurface reservoirs. A previous study showed that the dissolved gas extracted by headspace from the cores HD109 and a nearby core of HD319 consists only of methane, with $\delta^{13}C$ values of CH_4 ranging from -101.5‰ to -77.6‰ and from -77.8‰ to -57.8‰ below 100 cmbsf. This indicates that the external methane in the shallow sediments is of microbial origin (Fu, 2005). A comprehensive study indicated that microbial methane is predominant in the passive margin offshore southwestern Taiwan. The permeability of fluid channeling may determine the amount of microbial methane incorporated from shallow depth (Chen et al., 2017).

Profiles of Ba^{2+} concentration in pore fluids of the cores HD109 and HD319 resemble to those reported at other methane-rich systems, which are considered to be caused by barite precipitation slightly above or at the SMTZ (Torres et al., 1996; Dickens, 2001; Aloisi et al., 2004; Castellini et al., 2006; Snyder et al., 2007a; Snyder et al., 2007b; Vanneste et al., 2013). The modelling results for the data of Ba^{2+} show that the measured dissolved Ba^{2+} concentrations are lower than those predicted by the model above the SMTZ (Figure 4). These results indicate Ba^{2+} has been removed from the pore waters and taken up into the sediments as barite in sulfate-bearing layers above the SMTZ (Vanneste et al., 2013). The modern depth of active authigenic

barite generation just above the SMTZ is indicated by minima in porewater Ba^{2+} (Figure 2). Therefore, the solid-phase Ba front IV at core HD109 may denote an active authigenic barite front (Torres et al., 1996; Vanneste et al., 2013). Additionally, as the sulfate is absent in the pore fluids below the SMTZ, Ba^{2+} is most likely released after previous barite dissolution (Torres et al., 1996). In this case, there is no Ba front below the current SMTZ at the core HD109 (Figure 3), which confirms the dissolution of barite and release of Ba^{2+} in dissolved sulfate-free sediments. It is also supported by the modelling results, as the measured dissolved Ba^{2+} concentrations are higher than those predicted by the model at and below the SMTZ (Figure 4).

It is notable that there are obvious differences in the modelling results and the in-situ analytic results of solid phase POC, headspace CH_4, porewater SO_4^{2-} and Ca^{2+} (Figure 4). The modeled POC profiles do not match the measured one below ~50 cmbsf, possibly suggesting a non-steady POC deposition with various POC flux or/and sedimentation rate. The POC flux at sediment surface was often higher in the pre-Holocene period and thus more POC could be deposited at this time (Luo et al., 2015). In addition, the obvious differences between modelled and measured concentrations of CH_4 could be attributed to rapid degassing at the time of sampling (Feng et al., 2019, 2020). Since the porewater samples of the core HD109 were collected again for further study at intervals of 20 cm after the cruise, the unusually high SO_4^{2-} concentrations at the bottom of this core may be caused by the oxidation of dissolved sulfide produced by AOM after core retrieval (Lin et al., 2017). Dissolved hydrogen sulfide and solid-phase iron sulfide could be oxidized quickly to dissolved sulfate under aerobic and anaerobic conditions and lead to decreases in the porewater pH, further causing carbonate dissolution and Ca^{2+} release (Liu et al., 2019). Therefore, the occurrence of elevated Ca^{2+} concentrations at the bottom of the core HD109 may result from the dissolution of carbonate in the sediments. Despite some changes in the geochemical composition of pore fluids might occur before analysing the concentrations of major ions and trace elements, the redox zones and the major biogeochemical processes concerned in this study can still be identified according to the measured geochemical data.

Implications for the history of methane seepage

It is suggested that decline in the methane released flux could potentially verified by the formation of paleo-barite fronts located above the current position of the authigenic barite front (Dickens, 2001). Therefore, the diagenetic Ba enrichment is suggested to be useful to quantitatively trace the net downward movement of the SMTZ and the changes in upward methane flux due to its unique accumulation

mechanism (e.g., Dickens, 2001; Riedinger et al., 2006; Snyder et al., 2007a; Snyder et al., 2007b; Nöthen and Kasten, 2011; Kasten et al., 2012; Vanneste et al., 2013). The calculation results display that the Ba fronts at both cores have been accumulating since the last ten thousand years, including four episodes for several thousand years. In addition, substantial amounts of authigenic pyrites are also discovered at both cores. Most of the pyrite aggregates are black in color and tubular in shape, which consist of clustered framboids (Lu, 2007; Lin et al., 2017). A paragenetic sequence of pyrite crystal growth was observed at the core HD109, which starts as framboidal pyrite with numerous uniform microcrystals, followed by radial overgrowth, and later formed euhedral crystals (Lin et al., 2017). Three zones of ^{34}S enrichment in authigenic pyrites at the core HD109 (at 170 cmbsf, from 450 to 600 cmbsf, 730 to 765 cmbsf depth) show obvious offsets in respect to the present-day SMTZ, suggesting that these zones reflect the positions of paleo-SMTZ. Pyritization during diagenetic processes was revealed, as overgrowths and euhedral pyrite crystals have much higher δ^{34}S values in comparison with framboids (Lin et al., 2017). Moreover, the δ^{13}C values of bulk carbonate at core HD319 range from -2.04‰ to -0.02‰ and there is a negative excursion of $\delta^{13}C_{carbonate}$ at the bottom of the core, which suggests the addition of methane-derived authigenic carbonate into the sedimentary inorganic carbon pool within the current SMTZ (Lu, 2007).

In this study, the solid-phase Ba peaks together with the authigenic ^{34}S-enriched pyrite above the present-day SMTZ at the core HD109 both indicate that the sulfidization front was located closer to the seabed in the past (Lin et al., 2017). The uppermost Ba enrichment (Figure 3) implies that the SMTZ was once located at ~1.5 mbsf in the past. However, the depth distribution of the Ba fronts implies that the SMTZ migrated downward by ~4 m with time since the most intense methane seepage, leaving behind the accumulation of diagenetic barite. Hence, the estimations in this study suggest that intense methane seepage occurred around the Pleistocene/Holocene transition, then the upward methane flux have decreased episodically in the post-glacial period.

Indeed, because of sediment burial, the Ba fronts formed in the past would move downward subsequently after the downward migration of the SMTZ. Therefore, the "paleo" Ba fronts should have accumulated at shallower depths in the past. Given the sedimentation rates of 10 cm/kyr during MIS1 for core HD109 and HD319 (Chen et al., 2006), the shallowest "paleo" Ba fronts at ~1.5 mbsf at core HD109 and at ~3.3 mbsf at core HD319 should locate close to the seafloor when they were accumulating in about ten thousand years ago. Alternatively, the SMTZ may not move downward continuously but rather fluctuated over the sediment layer, given the intermittent characteristics of methane seepage and the possible pulses of upward methane flux in a highly dynamic condition (Lin et al., 2017).

Uranium-series ages of seep carbonates indicated that intensive seep activities intermittently occurred from 144.5 ± 12.7 ka to 11 ka in the northeastern SCS (Tong et al., 2013; Han et al., 2014; Feng and Chen, 2015; Chen et al., 2019; Maoyu Wang et al., 2022). The intensive seepage events occurred either during the times of sea-level lowstands or during the periods of sea-level fall before the LGM (Tong et al., 2013; Han et al., 2014; Yang et al., 2018). Previous studies suggest that gas hydrate decomposed during sea-level lowstands or falling stages due to decreases in hydrostatic pressure, and finally resulted in subsurface methane release and the SMTZ upward movements in the northern SCS (Tong et al., 2013; Han et al., 2014; Li et al., 2016; Lin et al., 2016; Xie et al., 2019). In the post-glacial period, the upward methane flux seemed to decrease significantly on a regional scale (Luo et al., 2015; Lin et al., 2016). However, intense seep activities also took place during the sea-level highstand at time of MIS 5e (133.3–112.7 ka BP) and MIS 1 (since 14 ka BP) (Feng and Chen, 2015; Liang et al., 2017; Chen et al., 2019). An increase in bottom water temperature likely triggered gas hydrate dissociation and associated methane seepage activities (Chen et al., 2019). Overall, the mechanisms for seepage activity are still under debated. More chronologic data of seep activities, especially the records of seepage during the deglaciation periods, are needed to better understand the forcing affecting seep activity.

In this study, the patterns of authigenic Ba fronts above the present-day SMTZ imply the downward migration of the paleo-SMTZ, while the estimation results suggest that the net decline in methane flux on the lower slope and at the bottom of the Taixinan Basin since about ten thousand years ago. Our modelling result shows that the released methane in shallow sediments was supplied from deeper sources, probably from underlying gas hydrate reservoir (Table 7). A study on a nearby sediment core (973–4) also indicated that the methane release flux had decreased since the last deglaciation, which was likely attributed to the decrease in the scale of gas hydrate decomposition (Zhang et al., 2018). The height of global sea level increased by more than 90 m since this period (Hanebuth et al., 2011). In theory, the rise of sea level led to an enhancement in the hydrostatic pressure and a decrease in the salinity, which further resulted in the thickening of the gas hydrate stability zone and the decline in the upward methane flux under a balanced pressure field (Sloan and Koh, 2007). Previous studies showed that even a moderate sea-level rise (<1 m) might significantly inhibit gas seepage at deep-water depths (>1,000 m) (Hsu et al., 2013; Sultan et al., 2020). In situ seafloor observations at the nearby cold seeps showed that the cold seeps in Jiulong Methane Reef and Haiyang four area were almost dormant at present day (Suess, 2005; Han et al., 2008; Huang et al., 2008; Wang et al., 2018). Therefore, the gradual decrease in upward methane flux on a regional scale is likely related to the stabilization of gas hydrate system in the northern SCS. This study suggest that

methane released fluxes in the northeastern SCS are highly variable both in spatial dimension and in temporal dimension, and provide new evidence in the driving mechanism of methane seepage in the post-glacial period.

Conclusion

In this study, we identify four intervals with authigenic barite front above the present-day SMTZ and use these Ba fronts to quantitatively track the net downward migration of the SMTZ at cores HD109 and HD319. Based on the estimation of the diffusive Ba^{2+} fluxes and the excess barium contents, microbial methane seepage probably occurred since about ten thousand years ago. It is proposed that methane seepage is more active during the LGM, inducing the SMTZ close to the seafloor. The upward methane flux then decreased and the SMTZ migrated downward gradually in hundreds to thousands of years in the post-glacial period. Consistent with other studies on the history of cold seep, our finding also imply that the gas hydrate system may be more stable during the post-glacial period in the northern SCS. This new case study indicates that methane seep activities on the northeastern slope of SCS are highly variable, and provides new insights on the evolution of methane seepage in the post-glacial period.

Data availability statement

The original contributions presented in the study are included in the article, further inquiries can be directed to the corresponding authors.

Author contributions

JF and NL conceived and designed the research, while JF wrote the manuscript. NL and ML analyzed the data and refined

the manuscript. JL, SY, and HW provided the metadata and funding. XS provided scientific supervision. All authors agree with the final version of the manuscript.

Funding

Conflict of interest

The authors declare that the research was conducted in the absence of any commercial or financial relationships that could be construed as a potential conflict of interest.

Publisher's note

All claims expressed in this article are solely those of the authors and do not necessarily represent those of their affiliated organizations, or those of the publisher, the editors and the reviewers. Any product that may be evaluated in this article, or claim that may be made by its manufacturer, is not guaranteed or endorsed by the publisher.

References

Aloisi, G., Wallmann, K., Bollwerk, S. M., Derkachev, A., Bohrmann, G., and Suess, E. (2004). The effect of dissolved barium on biogeochemical processes at cold seeps. *Geochim. Cosmochim. Acta* 68, 1735–1748. doi:10.1016/j.gca.2003.10.010

Bai, C., Zhang, G., Liang, J., Yang, Z., Yan, W., Zhu, D., et al. (2019). Deep-water sediment waves as a special gas hydrate reservoirs in the Northeastern South China Sea. *Mar. Pet. Geol.* 101, 476–485. doi:10.1016/j.marpetgeo.2018.12.031

Barnes, R. O., and Goldberg, E. D. (1976). Methane production and consumption in anoxic marine sediments. *Geol.* 4, 297–300. doi:10.1130/0091-7613(1976)4<297:mpacia>2.0.co;2

Berner, R. (1980). "Early Diagenesis: A theoretical approach," in *Princeton series in geochemistry* (Princeton, USA: Princeton University Press).

Boetius, A., Ravenschlag, K., Schubert, C. J., Rickert, D., Widdel, F., Gieseke, A., et al. (2000). A marine microbial consortium apparently mediating anaerobic oxidation of methane. *Nature* 407, 623–626. doi:10.1038/35036572

Boetius, A., and Wenzhöfer, F. (2013). Seafloor oxygen consumption fuelled by methane from cold seeps. *Nat. Geosci.* 6, 725–734. doi:10.1038/ngeo1926

Boudreau, B. P. (1997). *Diagenetic models and their implementation: Modelling transport and reactions in aquatic sediments.* Berlin, Germany: Springer, 414.

Burger, B. J., Estrada, M. V., and Gustin, M. S. (2019). What caused earth's largest mass extinction event? New evidence from the permian-triassic boundary in northeastern Utah. *Glob. Planet. Change* 177, 81–100. doi:10.1016/j.gloplacha.2019.03.013

Castellini, D. G., Dickens, G. R., Snyder, G. T., and Ruppel, C. D. (2006). Barium cycling in shallow sediment above active mud volcanoes in the Gulf of Mexico. *Chem. Geol.* 226, 1–30. doi:10.1016/j.chemgeo.2005.08.008

Chen, D., Huang, Y., Yuan, X., and Cathles, L. M. (2005). Seep carbonates and preserved methane oxidizing archaea and sulfate reducing bacteria fossils suggest recent gas venting on the seafloor in the northeastern South China Sea. *Mar. Pet. Geol.* 22, 613–621. doi:10.1016/j.marpetgeo.2005.05.002

Chen, F., Su, X., Lu, H., Zhu, Y., Liu, J., and Liao, Z. (2006). Lithologic features of sediments characterized by high sedimentation rates since the last glacial maximum from Dongsha area of the South China Sea. *Mar. Geol. Quat. Geol.* 26 (6), 9–17. (In Chinese with English abstract).

Chen, N. C., Yang, T. F., Hong, W. L., Chen, H. W., Chen, H. C., Hu, C., et al. (2017). Production, consumption, and migration of methane in accretionary prism of southwestern Taiwan. *Geochem. Geophys. Geosyst.* 18 (8), 2970–2989. doi:10.1002/2017gc006798

Chen, F., Wang, X., Li, N., Cao, J., Bayon, G., Peckmann, J., et al. (2019). Gas hydrate dissociation during sea-level highstand inferred from U/Th dating of seep carbonate from the South China Sea. *Geophys. Res. Lett.* 46 (23), 13928–13938. doi:10.1029/2019gl085643

Chuang, P. C., Dale, A. W., Wallmann, K., Haeckel, M., Yang, T. F., Chen, N. C., et al. (2013). Relating sulfate and methane dynamics to geology: Accretionary prism offshore SW Taiwan. *Geochem. Geophys. Geosyst.* 14 (7), 2523–2545. doi:10.1002/ggge.20168

Cui, H., Kaufman, A. J., Xiao, S., Zhou, C., Zhu, M., Cao, M., et al. (2021). Dynamic interplay of biogeochemical C, S and Ba cycles in response to the Shuram oxygenation event. *J. Geol. Soc. Lond.* 179 (2), 1–31. jgs2021-081. doi:10.1144/jgs2021-081

Dale, A. W., Regnier, P., Knab, N. J., Jørgensen, B. B., and Van Cappellen, P. (2008). Anaerobic oxidation of methane (AOM) in marine sediments from the skagerrak (Denmark): II. Reactiontransport modeling. *Geochimica Cosmochimica Acta* 72, 2880–2894. doi:10.1016/j.gca.2007.11.039

Dickens, G. R., Fewless, T., Thomas, E., and Bralower, T. J. (2003). "Excess barite accumulation during the Paleocene-Eocene Thermal Maximum: Massive input of dissolved barium from seafloor gas hydrate reservoirs," in *Causes and consequences of globally warm climates in the early paleogene*. Editior S. L. Wing, P. D. Gingerich, B. Schmitz, and E. Thomas (Boulder, Colorado, Geological Society of America Special Paper) 369, 11–23.

Dickens, G. R. (2001). Sulfate profiles and barium fronts in sediment on the blake ridge: Present and past methane fluxes through a large gas hydrate reservoir. *Geochim. Cosmochim. Acta* 65, 529–543. doi:10.1016/s0016-7037(00)00556-1

Dymond, J., Suess, E., and Lyle, M. (1992). Barium in deep-sea sediment: A geochemical proxy for paleoproductivity. *Paleoceanography* 7 (2), 163–181. doi:10.1029/92pa00181

Feng, D., and Chen, D. (2015). Authigenic carbonates from an active cold seep of the northern South China Sea: New insights into fluid sources and past seepage activity. *Deep Sea Res. Part II: Top. Stud. Oceanogr.* 122, 74–83. doi:10.1016/j.dsr2.2015.02.003

Feng, D., and Roberts, H. H. (2011). Geochemical characteristics of the barite deposits at cold seeps from the northern Gulf of Mexico continental slope. *Earth Planet. Sci. Lett.* 309, 89–99. doi:10.1016/j.epsl.2011.06.017

Feng, D., Qiu, J. W., Hu, Y., Peckmann, J., Guan, H., Tong, H., et al. (2018). Cold seep systems in the South China Sea: An overview. *J. Asian Earth Sci.* 168, 3–16. doi:10.1016/j.jseaes.2018.09.021

Feng, J., Yang, S., Wang, H., Liang, J., Fang, Y., and Luo, M. (2019). Methane source and turnover in the shallow sediments to the west of Haima cold seeps on the northwestern slope of the South China Sea. *Geofluids* ID1010824, 1–18. doi:10.1155/2019/1010824

Feng, J., Li, N., Luo, M., Liang, J., Yang, S., Wang, H., et al. (2020). A quantitative assessment of methane-derived carbon cycling at the cold seeps in the Northwestern South China Sea. *Minerals* 10 (3), 1–23. doi:10.3390/min10030256

Frieling, J., Peterse, F., Lunt, D. J., Bohaty, S. M., Sinninghe Damsté, J. S., Reichart, G. J., et al. (2019). Widespread warming before and elevated barium burial during the Paleocene-Eocene Thermal Maximum: Evidence for methane hydrate release? *Paleoceanogr. Paleoclimatol.* 34, 546–566. doi:10.1029/2018pa003425

Fu, S. (2005). Characteristics of the different hydrocarbon gases in marine sediments and their geochemical significances. *Earth Sci. Front.* 12 (3), 253–257.

Ge, L., Jiang, S. Y., Swennen, R., Yang, T., Yang, J. H., Wu, N. Y., et al. (2010). Chemical environment of cold seep carbonate formation on the northern continental slope of South China Sea: Evidence from trace and rare earth element geochemistry. *Mar. Geol.* 277, 21–30. doi:10.1016/j.margeo.2010.08.008

Gingele, F., and Dahmke, A. (1994). Discrete barite particles and barium as tracers of paleoproductivity in South Atlantic sediments. *Paleoceanography* 9, 151–168. doi:10.1029/93pa02559

Greinert, J., Bollwerk, S. M., Derkachev, A., Bohrmann, G., and Suess, E. (2002). Massive barite deposits and carbonate mineralization in the derugin basin, sea of okhotsk: Precipitation processes at cold seep sites. *Earth Planet. Sci. Lett.* 203 (1), 165–180. doi:10.1016/s0012-821x(02)00830-0

Griffith, E. M., and Paytan, A. (2012). Barite in the ocean–occurrence, geochemistry and palaeoceanographic applications. *Sedimentology* 59, 1817–1835. doi:10.1111/j.1365-3091.2012.01327.x

Han, X., Suess, E., Huang, Y., Wu, N., Bohrmann, G., Su, X., et al. (2008). Jiulong methane reef: Microbial mediation of seep carbonates in the South China sea. *Mar. Geol.* 249, 243–256. doi:10.1016/j.margeo.2007.11.012

Han, X., Suess, E., Liebetrau, V., Eisenhauer, A., and Huang, Y. (2014). Past methane release events and environmental conditions at the upper continental slope of the South China sea: Constraints by seep carbonates. *Int. J. Earth Sci.* 103, 1873–1887. doi:10.1007/s00531-014-1018-5

Hanebuth, T. J. J., Voris, H. K., Yokoyama, Y., Saito, Y., and Okuno, J. i. (2011). Formation and fate of sedimentary depocentres on Southeast Asia's Sunda Shelf over the past sea-level cycle and biogeographic implications. *Earth. Sci. Rev.* 104, 92–110. doi:10.1016/j.earscirev.2010.09.006

Hensen, C., Zabel, M., Pfeifer, K., Schwenk, T., Kasten, S., Riedinger, N., et al. (2003). Control of sulfate pore-water profiles by sedimentary events and the significance of anaerobic oxidation of methane for the burial of sulfur in marine sediments. *Geochim. Cosmochim. Acta* 67, 2631–2647. doi:10.1016/s0016-7037(03)00199-6

Holmkvist, L., Kamyshny, A., Vogt, C., Vamvakopoulos, K., Ferdelman, T. G., and Jørgensen, B. B. (2011). Sulfate reduction below the sulfate-methane transition in Black Sea sediments. *Deep Sea Res. Part I: Oceanogr. Res. Pap.* 58, 493–504. doi:10.1016/j.dsr.2011.02.009

Hong, W. L., Torres, M. E., Carroll, J., Crémière, A., Panieri, G., Yao, H., et al. (2017). Seepage from an arctic shallow marine gas hydrate reservoir is insensitive to momentary ocean warming. *Nat. Commun.* 8, 15745. doi:10.1038/ncomms15745

Hsu, S. K., Wang, S. Y., Liao, Y. C., Yang, T. F., Jan, S., Lin, J. Y., et al. (2013). Tide-modulated gas emissions and tremors off SW Taiwan. *Earth Planet. Sci. Lett.* 369, 98–107. doi:10.1016/j.epsl.2013.03.013

Hu, Y., Chen, L., Feng, D., Liang, Q., Xia, Z., and Chen, D. (2017). Geochemical record of methane seepage in authigenic carbonates and surrounding host sediments: A case study from the South China sea. *J. Asian Earth Sci.* 138, 51–61. doi:10.1016/j.jseaes.2017.02.004

Hu, Y., Luo, M., Liang, Q., Chen, L., Feng, D., Yang, S., et al. (2019). Pore fluid compositions and inferred fluid flow patterns at the Haima cold seeps of the South China Sea. *Mar. Pet. Geol.* 103, 29–40. doi:10.1016/j.marpetgeo.2019.01.007

Huang, Y., Suess, E., and Wu, N. (2008). *Methane and gas hydrate geology of the northern South China sea: Sino-German cooperative so-177 cruise report*. Beijing, China: Geological Publishing House.

Judd, A. G., and Hovland, M. (2007). *Submarine fluid flow, the impact on geology, biology, and the marine environment*. Cambridge, England: Cambridge University Press.

Kasten, S., Nöthen, K., Hensen, C., Spieß, V., Blumenberg, M., and Schneider, R. R. (2012). Gas hydrate decomposition recorded by authigenic barite at pockmark sites of the northern Congo Fan. *Geo-Mar. Lett.* 32, 515–524. doi:10.1007/s00367-012-0288-9

Kuang, Z., Fang, Y., Liang, J., Lu, J. A., and Wang, L. (2018). Geomorphological-geological-geophysical signatures of high-flux fluid flows in the eastern Pearl River Mouth Basin and effects on gas hydrate accumulation. *Sci. China Earth Sci.* 61, 914–924. doi:10.1007/s11430-017-9183-y

Li, L., Lei, X., Zhang, X., and Sha, Z. (2013). Gas hydrate and associated free gas in the Dongsha area of northern South China Sea. *Mar. Pet. Geol.* 39, 92–101. doi:10.1016/j.marpetgeo.2012.09.007

Li, L., Liu, H., Zhang, X., Lei, X., and Sha, Z. (2015). BSRs, estimated heat flow, hydrate related gas volume and their implications for methane seepage and gas hydrate in the Dongsha region, northern South China Sea. *Mar. Pet. Geol.* 67, 785–794. doi:10.1016/j.marpetgeo.2015.07.008

Li, N., Feng, D., Chen, L., Wang, H., and Chen, D. (2016). Using sediment geochemistry to infer temporal variation of methane flux at a cold seep in the South China Sea. *Mar. Pet. Geol.* 77, 835–845. doi:10.1016/j.marpetgeo.2016.07.026

Liang, Q., Hu, Y., Feng, D., Peckmann, J., Chen, L., Yang, S., et al. (2017). Authigenic carbonates from newly discovered active cold seeps on the northwestern slope of the South China Sea: Constraints on fluid sources, formation environments, and seepage dynamics. *Deep Sea Res. Part I: Oceanogr. Res. Pap.* 124, 31–41. doi:10.1016/j.dsr.2017.04.015

Lin, Q., Wang, J., Taladay, K., Lu, H., Hu, G., Sun, F., et al. (2016). Coupled pyrite concentration and sulfur isotopic insight into the paleo sulfate–methane transition zone (SMTZ) in the northern South China Sea. *J. Asian Earth Sci.* 115, 547–556. doi:10.1016/j.jseaes.2015.11.001

Lin, Z., Sun, X., Strauss, H., Lu, Y., Gong, J., Xu, L., et al. (2017). Multiple sulfur isotope constraints on sulfate-driven anaerobic oxidation of methane: Evidence from authigenic pyrite in seepage areas of the South China Sea. *Geochim. Cosmochim. Acta* 211, 153–173. doi:10.1016/j.gca.2017.05.015

Liu, C., Jiang, S., Su, X., Huang, C-Y., Zhou, Y., Bian, X., et al. (2019). An effective method to distinguish between artificial and authigenic gypsum in marine sedimentsffective method to distinguish between artifcial and authigenic gypsum

in marine sediments. *Mar. Pet. Geol.* 110, 706–716. doi:10.1016/j.marpetgeo.2019.07.044

Lu, H. (2007). *Mineralogical and geochemical studies on sediments from dongsha area, South China sea: Evidences for gas hydrate occurrence*. Dissertation. Sun Yat-sen University, 174.

Luo, M., Dale, A. W., Wallmann, K., Hensen, C., Gieskes, J., Yan, W., et al. (2015). Estimating the time of pockmark formation in the SW Xisha Uplift (South China Sea) using reaction-transport modeling. *Mar. Geol.* 364, 21–31. doi:10.1016/j.margeo.2015.03.006

Maoyu Wang, M., Chen, T., Feng, D., Zhang, X., Li, T., Robinson, L. F., et al. (2022). Uranium-thorium isotope systematics of cold-seep carbonate and their constraints on geological methane leakage activities. *Geochim. Cosmochim. Acta* 320, 105–121. doi:10.1016/j.gca.2021.12.016

McDonnell, S., Max, M., Cherkis, N., and Czarnecki, M. (2000). Tectono-sedimentary controls on the likelihood of gas hydrate occurrence near Taiwan. *Mar. Pet. Geol.* 17, 929–936. doi:10.1016/s0264-8172(00)00023-4

McManus, J., Berelson, W. M., Klinkhammer, G. P., Johnson, K. S., Coale, K. H., Anderson, R. F., et al. (1998). Geochemistry of barium in marine sediments: Implications for its use as a paleoproxy. *Geochim. Cosmochim. Acta* 62, 3453–3473. doi:10.1016/s0016-7037(98)00248-8

Naehr, T. H., Stakes, D. S., and Moore, W. S. (2000). Mass wasting, ephemeral fluid flow, and barite deposition on the California continental margin. *Geology* 28, 315–318. doi:10.1130/0091-7613(2000)028<0315:mweffa>2.3.co;2

Nöthen, K., and Kasten, S. (2011). Reconstructing changes in seep activity by means of pore water and solid phase Sr/Ca and Mg/Ca ratios in pockmark sediments of the Northern Congo Fan. *Mar. Geol.* 287, 1–13. doi:10.1016/j.margeo.2011.06.008

Paytan, A., Kastner, M., Martin, E. E., Macdougall, J. D., and Herbert, T. (1993). Marine barite as a monitor of seawater strontium isotope composition. *Nature* 366, 445–449. doi:10.1038/366445a0

Peckmann, J., Reimer, A., Luth, U., Luth, C., Hansen, B. T., Heinicke, C., et al. (2001). Methane-derived carbonates and authigenic pyrite from the northwestern Black Sea. *Mar. Geol.* 177, 129–150. doi:10.1016/s0025-3227(01)00128-1

Peckmann, J., and Thiel, V. (2004). Carbon cycling at ancient methane–seeps. *Chem. Geol.* 205, 443–467. doi:10.1016/j.chemgeo.2003.12.025

Riedinger, N., Kasten, S., Gröger, J., Franke, C., and Pfeifer, K. (2006). Active and buried authigenic barite fronts in sediments from the Eastern Cape Basin. *Earth Planet. Sci. Lett.* 241, 876–887. doi:10.1016/j.epsl.2005.10.032

Sauer, S., Crémière, A., Knies, J., Lepland, A., Sahy, D., Martma, T., et al. (2017). U-Th chronology and formation controls of methane-derived authigenic carbonates from the Hola trough seep area, northern Norway. *Chem. Geol.* 470, 164–179. doi:10.1016/j.chemgeo.2017.09.004

Schneider, A., Panieri, G., Lepland, A., Consolaro, C., Crémière, A., Forwick, M., et al. (2018). Methane seepage at Vestnesa Ridge (NW Svalbard) since the last glacial maximum. *Quat. Sci. Rev.* 193, 98–117. doi:10.1016/j.quascirev.2018.06.006

Schulz, H. D. (2006). "Quantification of early Diagenesis: Dissolved constituents in pore water and signals in the solid phase," in *Marine geochemistry* (Berlin, Heidelberg: Springer), 73–124.

Sloan, E. D., Jr., and Koh, C. (2007). in *Clathrate hydrates of natural GasChemical industries*. third ed. (CRC Press).

Snyder, G. T., Dickens, G. R., and Castellini, D. G. (2007a). Labile barite contents and dissolved barium concentrations on blake ridge: New perspectives on barium cycling above gas hydrate systems. *J. Geochem. Explor.* 95, 48–65. doi:10.1016/j.gexplo.2007.06.001

Snyder, G. T., Hiruta, A., Matsumoto, R., Dickens, G. R., Tomaru, H., Takeuchi, R., et al. (2007b). Pore water profiles and authigenic mineralization in shallow marine sediments above the methane-charged system on Umitaka Spur, Japan Sea. *Deep Sea Res. Part II: Top. Stud. Oceanogr.* 54, 1216–1239. doi:10.1016/j.dsr2.2007.04.001

Suess, E. (2005). *RV SONNE cruise report SO 177, sino-German cooperative Project, South China sea continental margin: Geological methane budget and environmental effects of methane emissions and gas hydrates*. IFM-GEOMAR Reports.

Sultan, N., Plaza-Faverola, A., Vadakkepuliyambatta, S., Buenz, S., and Knies, J. (2020). Impact of tides and sea-level on deep-sea Arctic methane emissions. *Nat. Commun.* 11, 1–10. doi:10.1038/s41467-020-18899-3

Tong, H., Feng, D., Cheng, H., Yang, S., Wang, H., Min, A. G., et al. (2013). Authigenic carbonates from seeps on the northern continental slope of the South China Sea: New insights into fluid sources and geochronology. *Mar. Pet. Geol.* 43, 260–271. doi:10.1016/j.marpetgeo.2013.01.011

Torres, M. E., Bohrmann, G., and Suess, E. (1996). Authigenic barites and fluxes of barium associated with fluid seeps in the Peru subduction zone. *Earth Planet. Sci. Lett.* 144, 469–481. doi:10.1016/s0012-821x(96)00163-x

Torres, M. E., McManus, J., and Huh, C. A. (2002). Fluid seepage along the san Clemente Fault scarp: Basin-wide impact on barium cycling. *Earth Planet. Sci. Lett.* 203, 181–194. doi:10.1016/s0012-821x(02)00800-2

Torres, M. E., Bohrmann, G., Dubé, T. E., and Poole, F. G. (2003). Formation of modern and Paleozoic stratiform barite at cold methane seeps on continental margins. *Geol.* 31, 897–900. doi:10.1130/g19652.1

Vanneste, H., James, R. H., Kelly-Gerreyn, B. A., and Mills, R. A. (2013). Authigenic barite records of methane seepage at the Carlos Ribeiro mud volcano (Gulf of Cadiz). *Chem. Geol.* 354, 42–54. doi:10.1016/j.chemgeo.2013.06.010

Von Breymann, M. T., Brumsack, H. J., and Emeis, K. C. (1992). *Proceedings of the ocean drilling Program scientific results*. in *Deposition and Diagenetic Behavior of Barium in the Japan Sea*, vol. 127/128. Ocean Drilling Program.

Wallmann, K., Aloisi, G., Haeckel, M., Obzhirov, A., Pavlova, G., and Tishchenko, P. (2006). Kinetics of organic matter degradation, microbial methane generation, and gas hydrate formation in anoxic marine sediments. *Geochim. Cosmochim. Acta* 70, 3905–3927. doi:10.1016/j.gca.2006.06.003

Wang, P., Prell, W. L., and Blum, P. (2000). *Proceedings of the ocean drilling Program*, initial reports, 184. Ocean Drilling Program.

Wang, X., Liu, B., Qian, J., Zhang, X., Guo, Y., Su, P., et al. (2018). Geophysical evidence for gas hydrate accumulation related to methane seepage in the Taixinan Basin, South China Sea. *J. Asian Earth Sci.* 168, 27–37. doi:10.1016/j.jseaes.2017.11.011

Wood, R. S., Lepland, A., Ogliore, R. C., Houghton, J., and Fike, D. A. (2021). Microscale δ³⁴S heterogeneities in cold seep barite record variable methane flux off the Lofoten-Vesterålen Continental Margin, Norway. *Earth Planet. Sci. Lett.* 574, 117164. doi:10.1016/j.epsl.2021.117164

Wu, S., Wang, X., Wong, H. K., and Zhang, G. (2007). Low-amplitude BSRs and gas hydrate concentration on the northern margin of the South China Sea. *Mar. Geophys. Res.* 28, 127–138. doi:10.1007/s11001-007-9020-y

Wu, D., Wu, N., Zhang, M., Guan, H., Fu, S., and Yang, R. (2013). Relationship of sulfate-methane interface (SMI), methane flux and the underlying gas hydrate in Dongsha area, northern South China Sea. *Earth Science–Journal China Univ. Geosciences* 38, 1309–1320. doi:10.1007/s11430-012-4545-6

Wu, N., Xu, C., Li, A., Cao, H., Chen, Y., Zhang, X., et al. (2022). Oceanic carbon cycle in a symbiotic zone between hydrothermal vents and cold seeps in the Okinawa Trough. *Geosystems Geoenvironment* 1 (3), 1–11. doi:10.1016/j.geogeo.2022.100059

Xie, R., Wu, D., Liu, J., Sun, T., Liu, L., and Wu, N. (2019). Evolution of gas hydrates inventory and anaerobic oxidation of methane (AOM) after 40ka in the Taixinan Basin, South China Sea. *Deep Sea Res. Part I: Oceanogr. Res. Pap.* 152, 103084. doi:10.1016/j.dsr.2019.103084

Xudong Wang, X., Guan, H., Qiu, J. W., Xu, T., Peckmann, J., Chen, D., et al. (2022). Macro-ecology of cold seeps in the South China sea. *Geosystems Geoenvironment* 1 (3), 1–11. doi:10.1016/j.geogeo.2022.100081

Yang, T., Jiang, S., Ge, L., Yang, J., Wu, N., Zhang, G., et al. (2010). Geochemical characteristics of pore water in shallow sediments from Shenhu area of South China Sea and their significance for gas hydrate occurrence. *Chin. Sci. Bull.* 55, 752–760. doi:10.1007/s11434-009-0312-2

Yang, K., Chu, F., Zhu, Z., Dong, Y., Yu, X., Zhang, W., et al. (2018). Formation of methane-derived carbonates during the last glacial period on the northern slope of the South China Sea. *J. Asian Earth Sci.* 168, 173–185. doi:10.1016/j.jseaes.2018.01.022

Yao, H., Niemann, H., and Panieri, G. (2020). Multi-proxy approach to unravel methane emission history of an Arctic cold seep. *Quat. Sci. Rev.* 244, 106490. doi:10.1016/j.quascirev.2020.106490

Zhang, G., Liang, J., Yang, S., Zhang, M., Holland, M., Schultheiss, P., et al. (2015). Geological features, controlling factors and potential prospects of the gas hydrate occurrence in the east part of the Pearl River Mouth Basin, South China Sea. *Mar. Pet. Geol.* 67, 356–367. doi:10.1016/j.marpetgeo.2015.05.021

Zhang, J., Lei, H., Chen, Y., Kong, Y., Kandasamy, S., Ou, W., et al. (2018). Carbon and oxygen isotope composition of carbonate in bulk sediment in the southwest Taiwan Basin, South China Sea: Methane hydrate decomposition history and its link to mud volcano eruption. *Mar. Pet. Geol.* 98, 687–696. doi:10.1016/j.marpetgeo.2018.08.031